Solar-Driven Reduction of Aqueous CO_2 with a Co Bis(terpyridine)-based Photocathode

Jane J. Leung‡, Julien Warnan‡, Khoa H. Ly, Nina Heidary, Dong Heon Nam, Moritz F. Kuehnel and Erwin Reisner*

Christian Doppler Laboratory for Sustainable SynGas Chemistry, Department of Chemistry, University of Cambridge, Lensfield Road, Cambridge CB2 1EW, United Kingdom

Email: reisner@ch.cam.ac.uk

‡These authors contributed equally.

ABSTRACT

The selective reduction of CO_2 with inexpensive solar-driven photoelectrochemical devices is a contemporary challenge in the quest for renewable fuel production. Here we report a molecular catalyst-based photocathode assembled from precious-metal-free components that is active towards solar-driven, aqueous CO_2 reduction. The reported photocathode is based on a phosphonated cobalt bis(terpyridine) catalyst that is interfaced *via* a mesoporous TiO_2 scaffold with a light-harvesting *p*-type silicon electrode. The hybrid photoelectrode reduces CO_2 to CO in both organic-water and purely aqueous conditions, achieving a turnover number of ~330 and maintaining stable activity for more than one day. Critically, in-depth electrochemical and *in situ* resonance Raman and infrared spectroelectrochemical investigations alluded to a catalytic mechanism that differs to that reported for the soluble metal bis(terpyridine) catalyst as the consequence of the immobilisation. In addition, it further unlocks an earlier catalytic onset and better electrocatalytic performance while enabling aqueous CO_2 reduction with the reported photocathode.

INTRODUCTION

The solar-driven conversion of CO_2 and water into renewable fuels and chemicals offers a promising route to storing the Sun's intermittent and diffuse energy.[1] However, achieving scalable and selective photoelectrodes for aqueous CO_2 conversion without generating hydrogen from competing proton reduction has yet to be accomplished.[2] CO_2-reducing molecular catalysts offer a distinct advantage over heterogeneous materials as they often combine high product selectivity with high efficiency, and their transparency ensures light penetration to allow for absorption by the supporting semiconductor.[3] On the other hand, photoelectrodes based on precious-metal-free heterogeneous catalysts for CO_2 reduction suffer from low selectivity, low Faradaic efficiencies (FE), and the inability to avoid competing hydrogen evolution in aqueous solution.[4] The immobilisation of molecular catalysts onto light-harvesting semiconductor photoelectrodes is an emerging approach in artificial photosynthesis to overcome these obstacles.[5] In contrast to most homogeneous photocatalytic systems, molecular photocathodes require no sacrificial electron source and only a minimal amount of catalyst, while utilising photoexcited electrons without the kinetic limitations of catalyst diffusion. However, only precious-metal-containing molecular photocathodes have been reported for aqueous CO_2 reduction to date,[6-10] the majority with formate ($HCOO^-$) over carbon monoxide (CO) as the predominant product.

This study reports a precious-metal-free molecular catalyst-based photocathode for aqueous CO_2 reduction. The photoelectrochemical hybrid system consists of a *p*-silicon (Si) photoelectrode modified with a mesoporous titania (mesoTiO_2) layer and adsorbed Co catalyst. Silicon is ubiquitous in the Earth's crust and its utilisation in the photovoltaic industry has resulted in a substantial price drop for crystalline Si in recent years.[11] Its conduction band (CB) energy delivers approximately 0.4 V for the reduction of CO_2 to CO and the small energy band gap (E_g) of 1.12 eV enables panchromatic light harvesting in the ultraviolet (UV), visible and near infrared (IR) region. The pivotal mesoTiO_2 interlayer provides a high surface area scaffold to enable high loading with a phosphonated cobalt(II)

bis(terpyridine) catalyst, **CotpyP** (Figure 1), as well as a substantial surface for contact with the electrolyte solution. Upon solar light irradiation, Si is able to inject electrons into TiO_2, which then shuttles them to the anchored Co catalyst. The hybrid photocathode performed CO_2 reduction in aqueous acetonitrile and purely aqueous electrolyte solution. The importance of the photocathode environment on the photoelectrocatalytic performance and mechanism was investigated by spectroelectrochemical IR and resonance Raman studies.

RESULTS

Photocathode Assembly

The CO_2-reduction catalyst **CotpyP** was synthesised by self-assembly of $Co(BF_4)_2 \cdot 6H_2O$ with two equivalents of phosphonated terpyridine (tpy), 2,2':6',2"-terpyridine-4'-phosphonic acid (**tpyP**). Full synthetic details and characterisation (^1H and ^{31}P nuclear magnetic resonance (NMR) spectroscopy, high-resolution mass spectrometry, IR and elemental analysis) are available in the Methods section and Supplementary Information. NMR spectroscopy is in agreement with previous reports of cobalt(II) bis(terpyridine) complexes, and no peaks for a potential Co mono(terpyridine) by-product were observed.[12] Attenuated total reflectance Fourier-transform IR (ATR-FTIR, Figure 2a) of the isolated **CotpyP** displayed bands at 1604, 1475, 1413 cm^{-1} (assigned to stretching vibrations of aromatic rings).[13] The UV-visible spectrum of **CotpyP** displays three absorption maxima (λ = 448, 510 and 555 nm in methanol), which have been previously attributed to metal-to-ligand charge (MLCT) transfer transitions for low-spin cobalt(II) bis(terpyridine) species (Supplementary Figure 1a-b).[14]

The Si|mesoTiO$_2$|**CotpyP** photocathode is assembled by first depositing a stabilising mesoporous, anatase TiO_2 scaffold (TiO_2 particle size ~15–20 nm, film thickness ~6 μm) on Si as previously reported (Supplementary Figure 2).[15] The Si|mesoTiO$_2$ electrodes were

subsequently modified with the catalyst by immersion in a methanol solution of **CotpyP**. UV-visible spectroscopic features for the adsorbed **CotpyP** were comparable to the isolated catalyst (Supplementary Figure 1b), suggesting that its structure is preserved upon immobilisation. Although the ATR-FTIR fingerprint region indicates the same catalyst core structure of the free and immobilised **CotpyP** (Figure 2a and Supplementary Figure 1c), the decrease in the intensity of bands near 1230 and 915 cm^{-1} (commonly attributed to ν(P=O) and ν(P–OH), respectively), together with shifts of the ν(P–Ar) at 1165 cm^{-1} and ν(P–O) bands around 1100-1000 cm^{-1} suggest the chemisorption of phosphonic acid upon adsorption on TiO_2.[16,17] X-ray photoelectron spectroscopy (XPS) showed binding signals in the Co_{2p}, P_{2p} and N_{1s} regions with elemental atomic concentration ratios in general agreement with the catalyst structure (Figure 2b-d, Supplementary Table 1). As a result of the TiO_2 scaffold's mesoporosity, a high loading of 45.0 ± 7.4 nmol cm^{-2} of chemisorbed **CotpyP** was achieved and quantified via inductively coupled plasma optical emission spectrometry after desorption (see Methods section for details).

Photoelectrocatalytic CO_2 Reduction

Controlled potential photoelectrolysis (CPPE) of Si|mesoTiO$_2$|**CotpyP** was conducted under a CO_2 atmosphere at an applied potential (E_{app}) of −1.0 V *vs.* Fc^+/Fc under continuous UV-filtered simulated solar irradiation (AM1.5G, 100 mW cm^{-2}, λ > 400 nm) at room temperature. CO and H_2 were quantified by gas chromatography, whereas $HCOO^-$ was quantified by ion chromatography. Different electrolyte solution compositions were studied to identify optimal conditions for the system. No CO_2 reduction products were detected with Si|mesoTiO$_2$|**CotpyP** in anhydrous acetonitrile (MeCN) containing 0.1 M tetrabutylammonium tetrafluoroborate ($TBABF_4$) after several hours of CPPE. Addition of water into the electrolyte solution resulted in catalytic CO_2 reduction with the turnover number ($TON_{CO_2} = TON_{CO} + TON_{HCOO^-}$) rising from 13 (9:1 v:v MeCN:H_2O) to 108 (7:3

MeCN:H_2O) after 8 h CPPE upon increasing the H_2O content. The product selectivity for CO was favoured over H_2 and formate in all cases and the overall FE (FE_{H_2} + FE_{CO} + FE_{HCOO^-}) increased from 12% (9:1 MeCN:H_2O) to 53% (7:3 MeCN:H_2O) (Figure 3 and Supplementary Table 2). The modest FE under these conditions can be partially attributed to initial parasitic reductive processes (as evidenced by an initial increase in the FE over time, see below), and ineffective catalyst reduction.[18] The latter is implied by the steadily decreasing turnover frequency for CO production (TOF_{CO}) over time (Supplementary Figure 3). Additionally, bare mesoTiO_2 electrodes are known to produce significant charging currents that do not translate into H_2 evolution in the absence of a catalyst.[15]

Further increase in water content increased the activity up to an optimal point of 40% water. In 6:4 MeCN:H_2O, a remarkably stable photocurrent as well as an overall FE of 77% (with FE_{CO} = 48%) and a TON_{CO_2} of 159 were achieved after 8 h CPPE (Figures 3 and 4a). The photocathode maintained activity during 24 h of operation and achieved a TON_{CO_2} of 381 (TON_{CO} = 334, TON_{HCOO^-} = 47, Supplementary Figure 4). An initial increase in the FE over time may once again be attributed to reduction of trapped O_2 in the mesoTiO_2 architecture,[19] while a gradual drop in FE over this long-term experiment may be a result of progressive desorption leading to unproductive transfer pathways. Bringing the water content to 50% also allowed for robust CPPE with a constant TOF_{CO} over time (Supplementary Figure 3), but a slightly reduced TON_{CO_2} and FE. Thus, increasing the water content in the electrolyte solution from 10-30% to 40-50% is beneficial for the photocathode performance.

The Si|mesoTiO_2|**CotpyP** photocathode was even found to display catalytic CO_2 reduction activity in pure CO_2-saturated water (0.1 M $KHCO_3$) at pH 6.7, reaching a TON_{CO_2} of 21 with a Faradaic efficiency for CO and $HCOO^-$ at 9.5% and 13% respectively after 8 h CPPE (Figure 3). Control experiments in the absence of either catalyst or CO_2 afforded no CO_2 reduction products and only minimal quantities of H_2 (Supplementary Figures 5 and 6). The catalytic selectivity changed from CO as the main product in hydro-organic media to proton-

containing formate and H_2 in purely aqueous electrolyte solution. Despite the TOF_{CO} being low, it remains constant during CPPE in water (Supplementary Figure 3), again implying good catalyst stability with an increasing presence of water. The latter is also supported by unaltered redox waves during repetitive cyclic voltammetry (CV) scans on a conductive oxide (*i.e.* indium tin oxide, ITO; Supplementary Figure 7 and more detailed discussion below).

Linear sweep voltammograms (LSVs) with chopped illumination in the optimal electrolyte solution (6:4 MeCN:H_2O) reveal a photocurrent onset potential at −0.44 V *vs.* Fc^+/Fc for Si|mesoTiO$_2$|**CotpyP**, compared to −0.56 V *vs.* Fc^+/Fc for the bare Si|mesoTiO$_2$ electrode (Figure 4b). **CotpyP**-functionalised photoelectrodes showed approximately double the photocurrent and an onset that occurs ~120 mV earlier. Note that the majority of charges in the **CotpyP**-free photoelectrode are charging of TiO_2 without promoting catalysis in the short timescale of LSVs (Supplementary Figure 8).[15]

Switching the Si photoelectrode for a supporting Ti foil substrate yields the equivalent dark Ti|mesoTiO$_2$|**CotpyP** electrode, whose LSVs (also recorded in CO_2-saturated 6:4 MeCN:H_2O conditions) display a current onset at approximately −1.0 V *vs.* Fc^+/Fc. This suggests that the photoabsorber delivers a photovoltage of ~550 mV (Supplementary Figure 9), in line with previous reports of Si photoelectrodes.[20] Controlled potential electrocatalysis (CPE) performed on the Ti|mesoTiO$_2$|**CotpyP** electrode at −1.0 V *vs.* Fc^+/Fc yielded no detectable products, further demonstrating the need for the light-absorbing Si electrode to operate at such a positive potential. Interestingly, the catalytic performances (current intensity, TON and selectivity) reached by the Si photoelectrodes at −1.0 V *vs.* Fc^+/Fc (Figures 3 and 4a) are matched only by the dark Ti-based electrodes when −1.3 V *vs.* Fc^+/Fc is applied during CPE (Supplementary Figure 10). Applying more positive or more negative potentials (E_{app} = −1.2 or −1.4 V *vs.* Fc^+/Fc, respectively) dramatically affect the CPE outcome, resulting in lower activity or selectivity towards CO (Supplementary Figure 10a). This potential dependency in product selectivity is in agreement with previous reports,[21] and

highlights the need for synergy between molecular catalyst and the photovoltage provided by the electrode. Furthermore, the comparable performances reached by Si|mesoTiO$_2$|**CotpyP** and Ti|mesoTiO$_2$|**CotpyP** at −1.0 and −1.3 V *vs.* Fc^+/Fc, respectively, suggest that kinetic limitations of the molecular catalyst **CotpyP** are the main factor determining performances, irrespective of the supporting electrode (Supplementary Figure 10b-c). Indeed, conducting light intensity dependent LSVs with Si|mesoTiO$_2$|**CotpyP** revealed a non-linear relationship between photocurrent density and light intensity (Supplementary Figure 11), further alluding to **CotpyP** being the kinetic bottleneck.

Several control experiments were conducted in 6:4 MeCN:H_2O solution to ascertain that CO_2 reduction catalysis originates from **CotpyP** (Figure 4c and Supplementary Figure 12). Product analysis following CPPE with both bare Si|mesoTiO$_2$ under CO_2 and Si|mesoTiO$_2$|**CotpyP** under N_2 revealed only traces of H_2 and no CO_2-reduction products (Supplementary Figures 13 and 14). Isotopic labelling experiments conducted with Si|mesoTiO$_2$|**CotpyP** in a $^{13}CO_2$-saturated solution confirmed that CO originated from CO_2 and not another carbon source (determined by gas-phase IR analysis; Supplementary Figure 15). CPPE was also conducted on a photoelectrode modified with the catalyst metal salt precursor, $Co(BF_4)_2{\cdot}6H_2O$ (Si|mesoTiO$_2$|$Co(BF_4)_2$; Supplementary Figure 16) to determine that CO_2 reduction was not being performed by Co salt released from the degrading molecular catalyst. The production of mostly H_2 at a FE of 84% and minimal CO and formate can be ascribed to catalysis carried out by a heterogeneous deposit.[22] Analyses by ATR-FTIR and XPS were further employed to confirm the post-CPPE molecular integrity of **CotpyP**. The FTIR fingerprint spectrum remained largely unchanged (Figure 2a), whereas the XPS spectra show clear signals at pre-CPPE binding energies and the absence of one at 778.2 eV in the Co_{2p} region that would indicate metallic Co (Figure 2b-d and Supplementary Table 1).[23] Only a small change in the atomic concentration ratios was observed, suggesting a small loss of the metal centre.

The inability of the immobilised **CotpyP** catalyst to turn over under anhydrous conditions implies a proton-dependent mechanism, but the substantial rate enhancements for CO_2 reduction up to 40% water content suggest an additional role of H_2O. Firstly, the enhanced catalytic rate with increasing H_2O content (TOF_{CO}, Supplementary Figure 3) is due to a changing thermodynamic landscape as $E°'(CO_2/CO)$ becomes less negative, resulting in a more exergonic reaction upon addition of protons (from water) to MeCN.[24] This change in $E°'(CO_2/CO)$ is most pronounced when the volume percentage of water (x) is $0 < x < 16$, and plateaus at $16 < x < 45$; our optimal conditions ($x = 40$) lies within this latter region. Secondly, (photo)electrocatalytic CO_2 reduction is commonly limited by its low solubility in solutions with high water content, partially explaining a performance maximum at a median water concentration.[25] This limited availability of CO_2 and the correspondingly higher concentration of protons would also favour H_2 evolution. Finally, as the water concentration increases in aprotic solvents, the proton adsorption-desorption equilibrium at the metal oxide electrode-solution interface favours proton adsorption.[26,27] This results in (i) a shift of the CB of TiO_2 to more positive potentials and (ii) changes in the surface hydrophilicity and local pH.[26,28,29] Consequently, the further addition of water in our system causes less thermodynamic driving force for both proton and CO_2 reduction and a more protic environment with a lower CO_2 concentration, resulting in less driving force for charge transfer to the catalyst as well as lower overall activity with reduced selectivity for CO_2 reduction.

Comparison with State of the Art

To date, reported molecule-based photocathodes performing CO_2 reduction remain scarce, whether in organic or water-containing media, and continue to rely on precious metal-containing components (Supplementary Table 3).[6-10,30-32] Moreover, even in anhydrous conditions where enhanced photocathode and/or catalyst stability may be expected, only a

few reports exist, and all depend on Re-based catalysts.[30-32] For instance, a Re-bipyridine catalyst on a Cu_2O photoelectrode protected by atomic layer deposited coatings has been reported to achieve a TON_{CO} of 70 in anhydrous MeCN.[32] Another benchmark system consists of a Ru-Re dye-catalyst dyad immobilised on NiO that evolves CO in dry dimethylformamide (DMF) solution.[30] Systems reported in water continue to face activity issues and favour H_2 and $HCOO^-$ over CO production. Apart from one that produces CO,[10] the few reports on narrow band gap semiconductors in water produce only formate with a TON_{HCOO^-} that does not exceed ~20,[6,7] and are all based on Ru-centred metal complex catalysts. Photoelectrochemical production of CO in aqueous solutions was achieved with Re- and Ru-centred catalysts, in dye-catalyst dyads on wide band gap semiconductors[8,9] or immobilised on a hematite photoelectrode,[10] respectively, with the maximum TON_{CO} in these systems reaching 125. In these CO-producing systems, H_2 and $HCOO^-$ also occurred as co-products – the former in quantities above half the amount of CO,[9] and the latter at similar proportions of CO[10] – demonstrating a continued struggle with product selectivity even with molecule-catalysed systems.

Despite not containing precious metals, the performance of our **CotpyP**-functionalised silicon photocathode exceeds all previous reports in both TONs towards CO_2-reduction products and stability.[6-10,30-32] Although the potential of Si as an earth-abundant light harvester has been recognised to drive homogeneous molecular catalysts for solar CO_2 reduction,[33-35] our work demonstrates the successful immobilisation of such a molecular catalyst onto Si to yield a discrete, functional photocathode from which CO_2 reduction products have been verified. This also allowed us to demonstrate CO production in pure water, which is an important milestone for precious-metal-free, synthetic molecular catalysts immobilised on a photocathode. Demonstrating aqueous CO_2 conversion for more than one day with the Co-centred molecular catalyst photo-driven by Si is an excellent basis for further improvement towards high-performance and scalable systems.

Notably, the performance of **CotpyP** in this photocathode also far exceeds that of any previously reported Co bis(terpyridine) catalyst – whether in solution or immobilised on dark electrodes – in terms of stability and activity.[36] This is even more remarkable when one recognises that the thermodynamic potential offered by the Si|mesoTiO$_2$ electrode ($E_{CB(TiO_2)}$ ~ −0.1 V *vs.* NHE) is rather small, especially when considering the significant overpotential previously reported for cobalt bis(terpyridine) complexes in solution (~ −2.0 V *vs*. Fc^+/Fc ≈ −1.4 V *vs*. NHE).[21,36] In order to gain a deeper understanding of the unexpected activity of our hybrid photocathode (*i.e.*, apparent mismatch of driving force provided by the photoelectrode and literature reports of the catalytic onset of cobalt bis(terpyridines)) and to provide an explanation for the strong solvent-dependent behaviour, detailed mechanistic investigations were executed by (spectro)electrochemical experiments.

Mechanistic Studies of Immobilised CotpyP

CV as well as potential-controlled ATR-IR and confocal resonance Raman (RR) studies were conducted on **CotpyP**-modified mesoporous ITO (mesoITO; particle size < 50 nm, film thickness 3 µm) electrodes. The complementarity of the two spectroscopic techniques delivers a global (ATR-IR) and specific (RR) monitoring approach to elucidate structural changes of the **CotpyP** catalyst under an applied potential. Thin mesoporous ITO electrodes (mesoITO) were elected to perform these experiments due to their conductivity, transparency and high molecular loading abilities that enable access to stronger (spectro)electrochemical signals across a wide potential range. A mechanistic interpretation is provided after presenting the results from these three techniques.

CV of mesoITO|**CotpyP** electrodes were recorded in 9:1 MeCN:H_2O (0.1 M $TBABF_4$) electrolyte solution under N_2 (Figure 5a and Supplementary Figure 17). An anodic sweep displays a reversible redox wave at $E_{1/2}$ = −0.12 V *vs*. Fc^+/Fc (***E*$_1$**) that can be assigned to the Co^{III}/Co^{II} redox couple.[21] Upon scan reversal towards negative potentials, a quasi-reversible

wave emerges at $E_{1/2}$ = −1.36 V *vs*. Fc^+/Fc (***E*₂**). The current density of this wave at ***E*₂** decreases upon consecutive scan cycles with the concomitant appearance of a new reversible redox wave at $E_{1/2}$ = −1.10 V *vs*. Fc^+/Fc (***E*₃**). In agreement with previous reports,[21] waves at ***E*₂** are assigned to the Co^{II}/Co^{I} redox couple and the emerging wave at ***E*₃** is therefore attributed to the formation of a Co^{II}/Co^{I} couple belonging to a new species that is more easily reduced than the original complex. Notably, although the anodic wave at ***E*₃** can already be observed in the first scan, the corresponding cathodic wave only appears in the second scan (Supplementary Figure 17). In contrast, the Co^{III}/Co^{II} couple at ***E*₁** remains largely unchanged throughout cycling. A comparable voltammetric behaviour is observed in 9:1 DMF:H_2O instead of MeCN:H_2O (Supplementary Figure 18), indicating that the organic solvent does not seem directly responsible for the couple at ***E*₃**.

Increasing the water content of the electrolyte solution sequentially from 9:1 to 6:4 (MeCN:H_2O mixtures) results in faster growth of the ***E*₃** redox couple (Figure 5b), which points towards a water/proton-involving process for the formation of the new species. Notably, running CV after removing the applied potential (at an open circuit potential of ~ −0.5 V *vs*. Fc^+/Fc) following an initial set of consecutive scans in 9:1 MeCN:H_2O showed the same voltammetric response as the original 1st scan (Figure 5a, compare scans 7 and 8). The latter behaviour suggests that the process is only accessible in 9:1 MeCN:H_2O if certain conditions induced by electrode polarisation are met; these are discussed further below.

CV of mesoITO|**CotpyP** under a CO_2 atmosphere show a catalytic onset reduction wave (E_{cat} ~ −1.3 V *vs*. Fc^+/Fc) that is more pronounced in 6:4 MeCN:H_2O compared to 9:1 MeCN:H_2O (Supplementary Figure 19b), which is consistent with its better activity in our CPPE results above. Notably, the catalytic onset potential occurs ~700 mV earlier than those generally reported for Co bis(terpyridine) catalysts in solution.[21]

Confocal RR spectroelectrochemistry was employed to investigate the potential-dependent features of the adsorbed catalyst at a molecular level *in situ* using 413, 458, and 514 nm

excitation wavelengths (λ_{ex}) to match the strong MLCT transitions of Co bisterpyridine complexes, including those of **CotpyP** (Supplementary Figure 1a-b). The RR spectra of dry mesoITO|**CotpyP** (in absence of solution) were dominated by bands located at 1345, 1473 and 1603 cm^{-1} with altered relative intensities depending on the employed excitation wavelength (Supplementary Figure 20; characteristic frequencies given in Supplementary Table 4) and are consistent with previous reports for terpyridine-based complexes.[37,38] The high RR intensities are attributed to the high effective surface area resulting from the mesoporous electrode architecture,[37,39] and the strong electronic absorption of the complex in the visible spectrum.[40] The spectrum of the dry mesoITO|**CotpyP** electrode matches that of the **CotpyP** powder and not a cobalt mono(terpyridine) (Supplementary Figure 21a and Supplementary Table 4). Conservation of the structural bis-ligation upon placing the electrode in 9:1 MeCN:H_2O solution (0.1 M $TBABF_4$) is indicated by an unchanged RR band pattern (Supplementary Figure 21b). Potential-dependent confocal RR spectra of mesoITO|**CotpyP** were subsequently recorded at E_{app} between 0.5 and −1.6 V *vs*. Fc^+/Fc (Figure 6a). At positive potentials, a weakly pronounced spectral pattern with major bands located at 1561 (not specifically labelled) and 1611 cm^{-1} was observed (Supplementary Table 5). Lowering E_{app} below 0.0 V *vs*. Fc^+/Fc caused the disappearance of these bands with a concomitant rise of intense bands at 1345, 1483, 1542 and 1603 (not specifically labelled) cm^{-1}, which are in good agreement to those for the native [Co^{II}] state in the **CotpyP** powder (Supplementary Figure 21a). Further lowering E_{app} below −1.0 V *vs*. Fc^+/Fc resulted in bands rising at 1466, 1556 and 1593 cm^{-1} attributed to the [Co^{I}] state, with the simultaneous disappearance of the aforementioned **Co^{II}tpyP** bands. As these changes were all fully reversible upon changing the potential-step direction, they do not suggest irreversible alteration of the complex over the broad potential window.

The potential-dependent RR spectra of mesoITO|**CotpyP** over the full potential window could be fitted accurately using three component spectra (Supplementary Figure 22; see Methods section for a detailed description). One of the component spectra fully resembles

the RR spectrum obtained for the dry mesoITO|**CotpyP** electrode (in absence of solution; Supplementary Figures 20 and 21b). To confirm that the spectral components can indeed be assigned to three Co oxidation states, relative intensities of the components were plotted against E_{app}. This approach resulted in matching sigmoidal curves that indicate complete interconversion from one oxidation state to another (Figure 6b). The apparent redox potentials can be estimated from the inflection points of the sigmoidal curves (−0.18 and −1.32 V *vs.* Fc^+/Fc), and match those determined for Co^{III}/Co^{II} (***E*₁**) and Co^{II}/Co^{I} (***E*₂**) from voltammetric experiments (Figure 5).

Measurements recorded in CO_2-saturated conditions revealed the same spectral patterns as observed under N_2 (Supplementary Figure 23). Lowering E_{app} to the catalytic region of −1.6 V *vs*. Fc^+/Fc, followed by stepping back to 0.5 V *vs*. Fc^+/Fc once again demonstrated full reversibility of the spectral features. Holding E_{app} at −1.4 V *vs*. Fc^+/Fc for 10 min resulted in no significant alteration of the **Co^{I}tpyP** spectrum. Both observations point to preservation of the complex's overall molecular structure and its metal's first coordination sphere, as either loss of a terpyridine ligand or changes in the hapticity of the complex would have afforded significant alterations of the RR spectral pattern and relative intensities (see Supplementary Figure 21a). This highlights the maintained structural integrity of **CotpyP** even after catalytic turnover, which is consistent with the CV and post-CPPE XPS and ATR-IR measurements above. It is however noted that catalytic intermediates that involve opening the coordination sphere are unlikely to be detectable in our experiment's timeframe due to their transient nature.

Interestingly, we noted a singular band at 1546 cm^{-1} that exhibits altered intensities at potentials more negative than −1.0 V *vs*. Fc^+/Fc (*i.e.* [Co^{I}]-affording) under N_2 and CO_2 atmospheres (Supplementary Figure 24). Component fit analysis showed that this band exhibits a different potential-dependence to that of **Co^{I}tpyP**, suggesting that it involves a vibrational mode that is sensitive to a potential-coupled process other than mere reduction. Further, this band was more pronounced in anhydrous MeCN electrolyte solution, while

adding H_2O (9:1 MeCN/H_2O, 0.1 M $TBABF_4$) resulted in a strong decrease in its intensity. In contrast, replacing H_2O with D_2O afforded only minor changes in this band compared to spectra recorded in anhydrous MeCN. Isotopically induced shifts were not observed in the marker band (Supplementary Figure 25a, b, d). On the other hand, adding DCl (95 µM) to the 9:1 MeCN:D_2O solvent induced a decrease in the band's intensity analogous to that observed when H_2O was added to MeCN (Supplementary Figure 25c-d). Overall, it is evident that the band at 1546 cm^{-1} is sensitive to the apparent acidity of the solution, and would suggest a dependence on a proton-containing function. From these observations and due to the frequency of the band, it appears likely that the 1546 cm^{-1} band reflects ν(C=N) and ν(C=C) pyridine ring modes sensitive to the electronic density at the cobalt atom and is therefore also affected by the electronic effect induced by the phosphonic acid group's protonation state. Substituents in the *para* position in pyridine-coordinated complexes have been shown to exert a strong effect on the electron density at the coordinated metal atom.[41] In this respect, the retained intensity of the band at 1546 cm^{-1} in the case of these D_2O experiments could be explained by a lack of shift of the protonation equilibrium of the phosphonic acid groups as a result of the lesser acidity of D_2O compared to H_2O.

ATR-IR spectroelectrochemical measurements were also conducted under varying applied potentials, beginning at E_{app} = −0.5 V *vs.* Fc^+/Fc ([Co^{II}]-affording potential) and proceeding step-wise from E_{app} = −1.0 V through to −1.5 V *vs.* Fc^+/Fc ([Co^{I}]-affording potential; Supplementary Figure 26). In agreement with RR experiments, ATR-IR measurements in dry N_2, wet N_2 and wet CO_2 conditions likewise did not detect changes in **CotpyP**'s primary coordination sphere. This is indicated by the similar spectral changes under non-catalytic and catalytic conditions as observed in the second derivative and difference spectra of the absorbance in the aromatic terpyridine spectral region (blue regions of Supplementary Figures 27 and 28, respectively). More specifically, additional new bands do not arise in the aromatic region upon applying potentials in different solvent media. The spectra display only mild intensity changes and the few band shifts (e.g., at 1458 cm^{-1} and 1390 cm^{-1}

characteristic of pyridine ring modes) cannot account for either changes in the hapticity or complete loss of the terpyridine ligands.

Nonetheless, spectroelectrochemical ATR-IR allowed us to probe media-dependent changes specifically in the phosphonate spectral region, affording a qualitative means to monitor their role *in situ* under applied potentials. As can be seen from the absorbance spectra, addition of H_2O (Supplementary Figure 26b) and, further, CO_2 (Supplementary Figure 26c) results in broadening of the band features in the phosphonate region – shown between 1250 and 900 cm^{-1}, corresponding to contributions from the acid's stretching frequencies[42] – indicating a change at the phosphonate group that would be in line with protonation at this site, as previously reported in ATR-IR studies.[42,43] Nevertheless, the broad band features of the phosphonate region are best deconvoluted into their discrete components by computing the second derivatives (Figure 7) of the absorbance spectra. While only a few minor changes in band intensities within this phosphonate region were observed upon reducing **Co^{II}tpyP** to **Co^{I}tpyP** under dry MeCN conditions (Figure 7a), the addition of water in 9:1 MeCN:H_2O, N_2-purged electrolyte solution led to large spectral changes at [Co^{I}]-affording potentials across the entire phosphonate region (Figure 7b).[42,43] For instance, changing intensities of bands reflective of ν(P−O) and ν(P−OH) phosphonate vibrational modes are observed (decrease at 1126, 1082 and 965 cm^{-1}; increase at 1168 and 1011 cm^{-1}). Under CO_2, similar but significantly weaker changes to that found under wet N_2-purged conditions were also observed when lowering E_{app} down to catalytic conditions (Figure 7c). Overall, these observed trends are supportive of a change in protonation of the phosphonate group upon addition of water under N_2, which is later revoked during catalysis in presence of CO_2 due to a difference in the protonation state of the observed steady-state species.

Spectroscopic and electrochemical evidence suggests that the complex's bis(terpyridine) ligation is preserved under (photo)electrocatalytic CO_2 reduction, and that catalysis does not involve irreversible structural alteration to the metal's first coordination sphere (Figures 2, 5a, 6a and Supplementary Figure 23). Considering that the immobilised **CotpyP** displays an

onset for CO_2 reduction at a much more positive potential than that previously observed in solution, and that formate has previously been the only product from cobalt bis(terpyridine)-catalysed CO_2 reduction in water,[44] we propose that the mechanism in our system proceeds differently to that commonly reported for metal bis(terpyridine) complexes.[21,36] Specifically, the catalytic mechanism of our immobilised **CotpyP** species involves retention of the bis-tpy ligation, whereas previous reports of homogeneous Co bis(terpyridine)s suggested that they proceed *via* the irreversible loss of one terpyridine ligand to generate a Co(I) mono(terpyridine).[21] This difference is depicted in Figure 8, which presents structures of both (spectro)electrochemically-supported (**A**, **B**, **C**) and speculated (**D**) molecular species, as discussed below.

The existence of an alternative mechanism for immobilised **CotpyP** is also indicated by the emergence of waves at $\boldsymbol{E_3}$, which has not been previously reported for cobalt bis(terpyridine)s. Moreover, the latter occurs at a potential just prior to that of the CO_2-reduction catalytic onset (Figure 5 and Supplementary Figure 19), suggesting that the $\boldsymbol{E_3}$-related species is non-innocent towards CO_2 reduction. In light of the nature of the changes observed in the RR and ATR-IR spectra, it is probable that all chemical processes resulting from the redox steps at $\boldsymbol{E_1}$, $\boldsymbol{E_2}$ and $\boldsymbol{E_3}$ occur without major disruption of the Co coordination sphere, thereby ruling out ligand exchange possibilities. Rather, CV, RR and ATR-IR measurements suggest a proton-involving pathway that likely involves the unbound phosphonate group of the [Co^{I}] complex. From these observations, we propose that the species formed at $\boldsymbol{E_3}$ is a [Co^{I}] complex bearing a diprotonated phosphonic acid (Figure 8, species **C**). We deduce that species **C** can be generated either *via* a proton-coupled electron transfer process (PCET) from **A** or *via* a chemical step from **B**, depending on the water content of the electrolyte solution. The former mechanism was observed at $\boldsymbol{E_3}$ in early CV scans in water-rich solution, whereas **C** required several CV scans to become significantly apparent in water-deficient medium. The promotion of **C**'s formation by the presence of protons can be further supported by: (i) the diminishing of the RR band at 1546 cm^{-1} for [Co^{I}]

(typically observed in anhydrous MeCN conditions) and (ii) changes in phosphonate group IR frequencies upon addition of water or acid as a result of the protonation of the unbound phosphonate. This can be rationalised in two ways: (i) by the presumed increased basicity of the phosphonate group in the [Co^{I}] state as the π-symmetry of the filled Co d-orbital is suggested to allow the electronic density to spread on the π^* levels of the terpyridine (a relatively good π-acceptor)[13] and diminish its electron-withdrawing effect on the phosphonate group, and (ii) by the phosphonic acid's increasing pK_a or decreasing local pH with negative polarisation of the electrode from the surface potential effect.[45,46]

We attribute the slow growth of $\boldsymbol{E_3}$ in water-poor media to a steady increase of the local proton concentration at the electrode-solution interface upon cycling (as previously observed for metal oxides), which favours the PCET mechanism and further allows for the observed cycle-dependent behaviour in Supplementary Figure 17.[47,48] This hypothesis is supported by the disappearance of wave $\boldsymbol{E_3}$ upon restoring the electrode to its initial state by allowing equilibration at open-circuit conditions (Figure 5a). As such, in such a water-poor medium, we attribute the origin of the oxidation wave of **C** seen in the first scan to the protonation of **B**.

On the other hand, the formation of species **C** is promoted upon increasing the acidity of the medium (by increasing water content and/or purging with CO_2), with the catalytic potential towards CO_2 reduction close to the potential of the formation of species **C** (Figure 5 and Supplementary Figure 19). These observations ultimately suggest that **C** is involved in the CO_2 reduction mechanism and we thus postulate that, upon reduction of the complex and coordination of CO_2, **D** is a plausible CO-releasing intermediate. Its formation would involve the de-coordination of one or two pyridines to create a vacant coordination site and, subsequently, the oxidative addition of CO_2.[49] In fact, the d^8 configuration of [Co^{I}] species is likely to favour a square planar or tetrahedral geometry, as well as increase the lability of the ligand.[50,51] Moreover, the pyridine de-coordination is likely to be stabilised by protonation of its nitrogen atom from the diprotonated phosphonic acid due to the latter's lower pK_a value.[52]

As a result, the deprotonated phosphonic acid could in effect act as a proton relay or H-bond source, facilitating C-O bond cleavage during catalysis. The formation of such a stabilising intermediate would also explain why CO is formed as the major catalytic product at the expense of formate (the only previously-observed CO_2 reduction product in analogous homogeneous conditions) and H_2, both of which would have required the stabilisation of a Co-H intermediate instead. At this stage, it is difficult to adjudicate whether CO_2 insertion would occur in **C** or only after further reduction of **C**. It is also worth noting that, in the absence of time-resolved experiments, this interpretation does not rule out the possibility that **B** could, upon further reduction, permit CO_2 reduction without necessarily involving **C** and **D** in the mechanism, and the suggested mechanism remains tentative. Nevertheless, the suggested mechanistic pathway contrasts overall with previous reports and suggests exciting benefits of immobilising a metal complex (such as the opportunity to operate in an aqueous solution) that are not accessible in analogous homogeneous systems.[44,50,53]

CONCLUSIONS

We report a precious-metal-free molecular photocathode towards solar-driven CO_2 reduction. This Si|mesoTiO$_2$|**CotpyP** electrode is active towards CO and formate production in both hydro-organic and purely aqueous solution, achieving a TON for CO_2-reduction products as high as 381 after 24 h – exceeding previously reported benchmarks for molecular photocathodes (including those containing precious metal complexes). Furthermore, with a selectivity towards CO making up ~75% of all gaseous products, our photocathode compares favourably with most reported precious-metal-free photocathodes based on heterogeneous catalysts that deliver state-of-the-art performances. Our results further highlight that altering the water content of the photoelectrocatalysis media has a pronounced effect on the stability, activity, and product selectivity of the photocathode.

Intriguing insights into how the catalyst is permitted to enter its reduced and pre-catalytic state were obtained by cyclic voltammetry as well as *in situ* ATR-IR and RR spectroelectrochemical experiments. The formation of a key intermediate (species **C**) is revealed that creates an alternative CO_2 reduction mechanism without requiring the loss of one terpyridine, which is in sharp contrast to the conventional understanding for metal bis(terpyridine) catalysts in solution. This unexpected mechanistic pathway enabled **CotpyP** to perform CO_2 reduction on Si|mesoTiO_2 thanks to a dramatically lower catalytic onset (700 mV), and consequently led to improved stabilities and a TON four times higher than previously reported for Co terpyridine complexes.[36] This unexpected performance enhancement was ultimately afforded by the synergy of having a phosphonic acid functional group alongside the possibility to operate the system under aqueous conditions – the latter having been conferred by the catalyst's immobilisation. In addition to shedding insight on the behaviour of the complex, these experiments also illustrate the power and precision offered by *in situ* vibrational spectroscopic techniques in the wider context of better understanding molecular catalyst-based solar fuel devices.

FIGURES

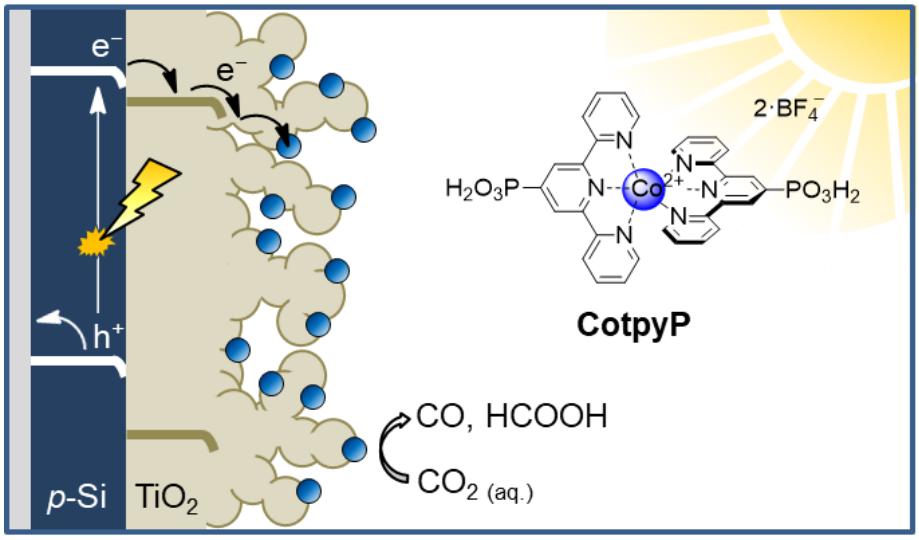

Figure 1. Schematic representation of Si|mesoTiO$_2$|**CotpyP** photocathode (not drawn to scale).

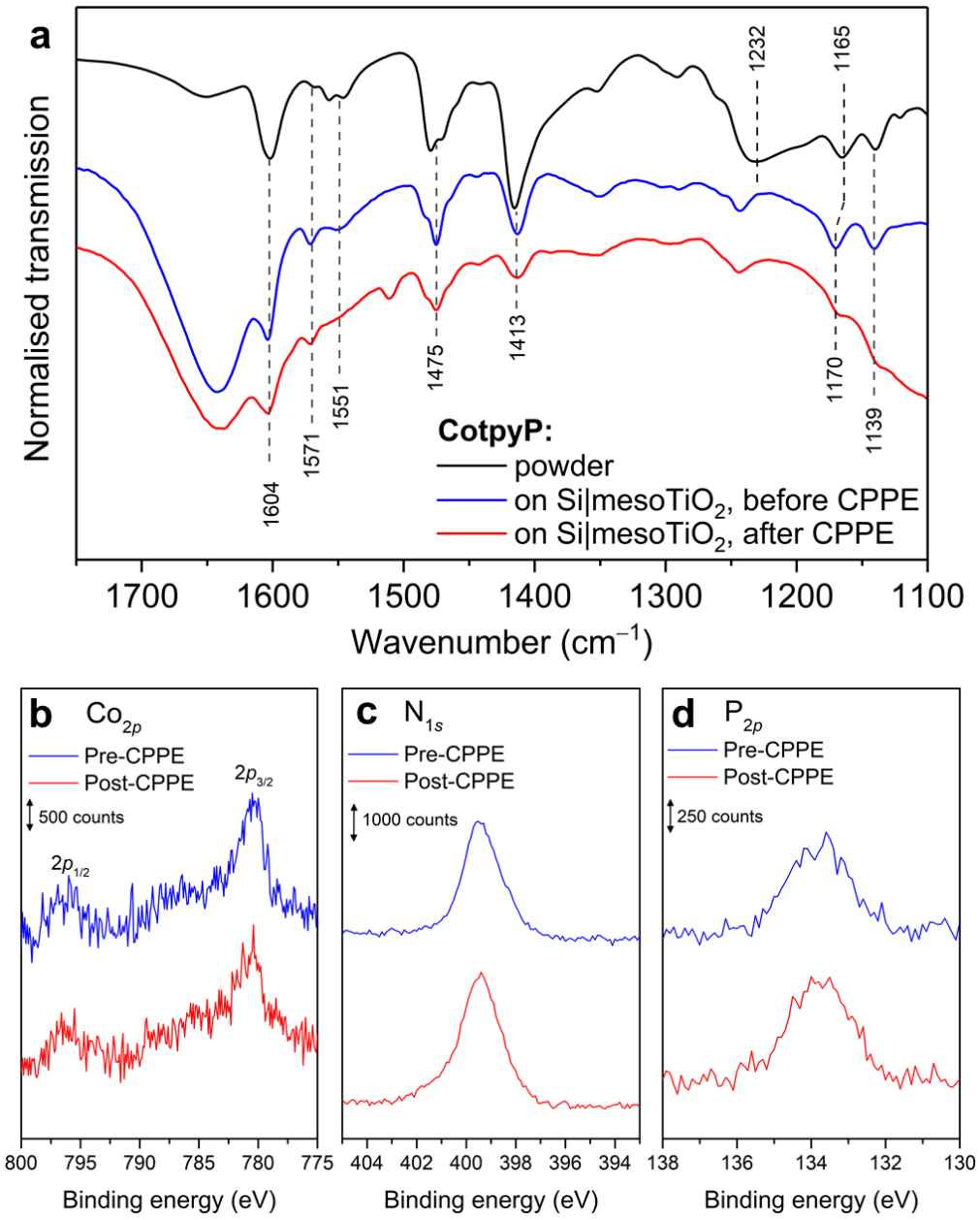

Figure 2. Characterisation spectra of **CotpyP** before and after CPPE. (a) ATR-FTIR spectra of **CotpyP** as powder (black trace), and after immobilisation on mesoTiO$_2$ before (blue trace) and after (red trace) 1 h of CPPE. (b-d) XPS spectra of Si|mesoTiO$_2$|**CotpyP** in the Co$_{2p}$, N$_{1s}$ and P$_{2p}$ regions showing peaks attributed to Co^{II}-N, pyridine N and phosphonic acid groups, respectively, before (black traces) and after (red traces) 8 h of CPPE. CPPE conditions: E_{app} = −1.0 V *vs.* Fc$^+$/Fc, 1 Sun (AM1.5G, 100 mW cm^{-2}, λ > 400 nm), CO$_2$-saturated conditions in 6:4 MeCN:H$_2$O with 0.1 M TBABF$_4$ at room temperature.

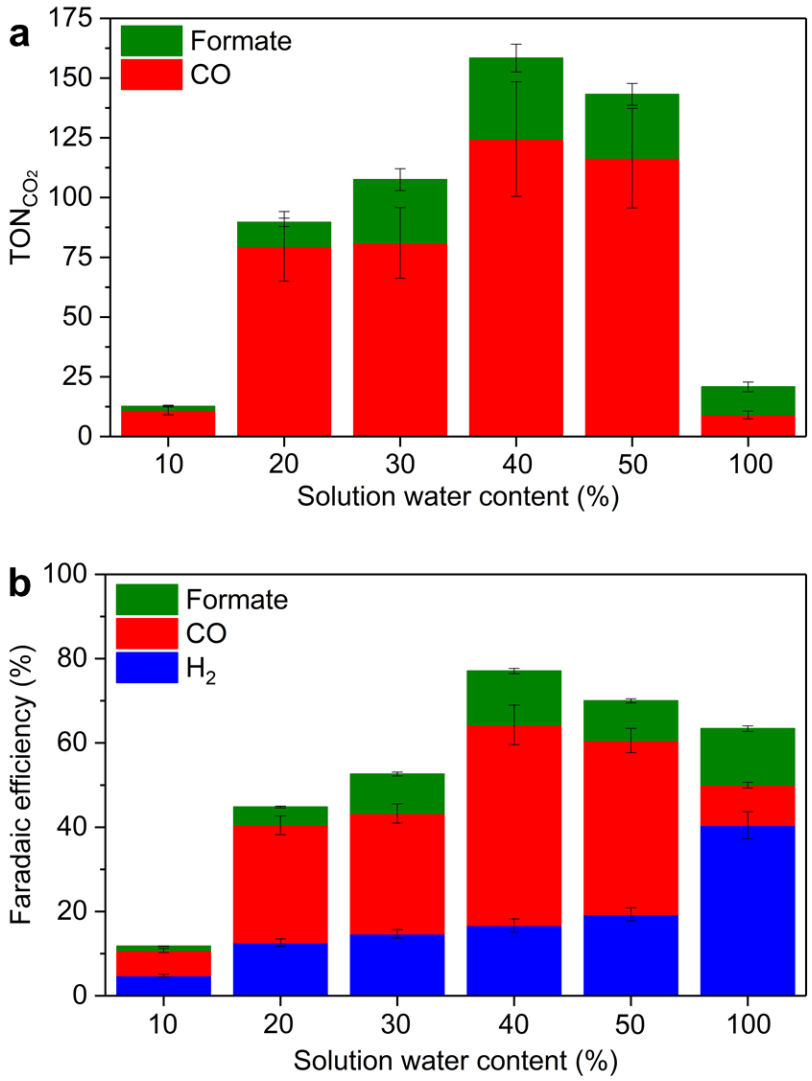

Figure 3. Performance of Si|mesoTiO$_2$|**CotpyP** photocathodes in different electrolyte solutions after 8 h of CPPE. (a) TON for CO_2 reduction products (TON_{H_2} not included as catalyst-free Si|mesoTiO$_2$ photoelectrode produces small amounts of H_2; see Supplementary Figure 13) and (b) FEs (cumulative over the duration of the CPPE) for all products. Conditions: E_{app} = −1.0 V *vs.* Fc^+/Fc for MeCN:H_2O mixtures, E_{app} = 0.0 V *vs.* RHE for H_2O; simulated solar light (AM1.5G, 100 mW cm^{-2}, λ > 400 nm); CO_2-saturated solutions of $TBABF_4$ (0.1 M) in MeCN:H_2O mixtures (solution water content 10-50%) or $KHCO_3$ (0.1 M) in pure water; room temperature. A tabulated summary of results is available in Supplementary Table 2. Error bars correspond to the standard deviation (n = 3).

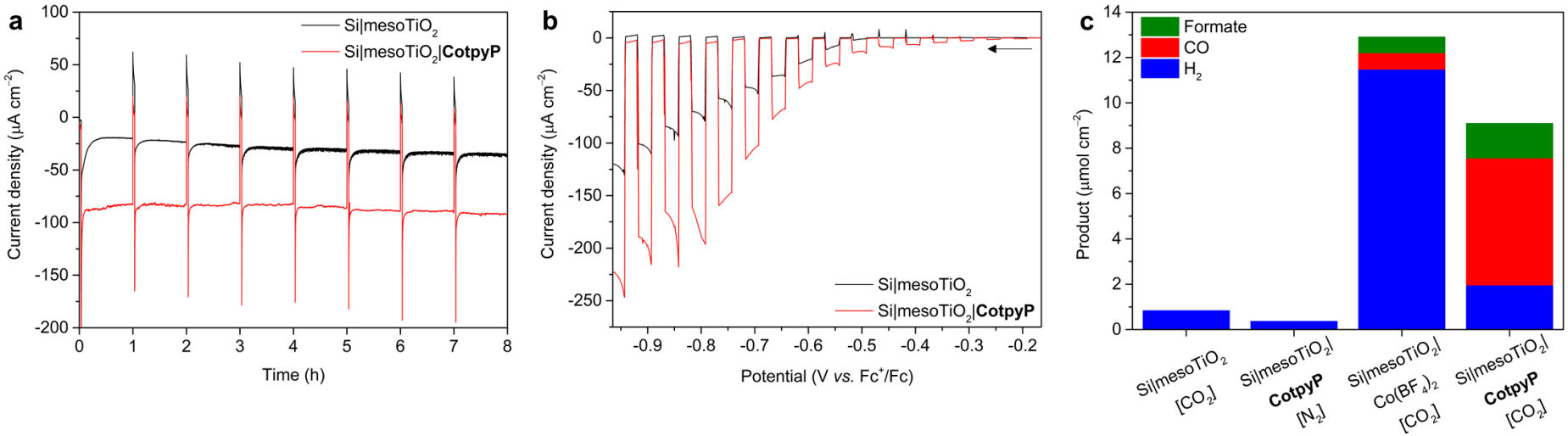

Figure 4. Photoresponse of Si|mesoTiO$_2$|**CotpyP** in catalytic conditions and control experiments. (a) CPPE (*J*-*t*) traces (E_{app} = −1.0 V *vs.* Fc$^+$/Fc, CO$_2$-saturated conditions) with Si|mesoTiO$_2$ (black trace) and Si|mesoTiO$_2$|**CotpyP** (red trace) photocathodes under continuous illumination and an hourly 2 min dark chop (for close-up see Supplementary Figure 8). (b) LSVs of Si|mesoTiO$_2$ and Si|mesoTiO$_2$|**CotpyP** with chopped illumination (v = 5 mV s^{-1}, CO$_2$-saturated conditions); the arrow indicates scan start. (c) Product analysis from Si|mesoTiO$_2$|**CotpyP** and control experiments after 8 h of CPPE (E_{app} = −1.0 V *vs.* Fc$^+$/Fc). Conditions: 6:4 MeCN:H$_2$O with TBABF$_4$ (0.1 M); 1 Sun (AM1.5G, 100 mW cm^{-2}, λ > 400 nm); room temperature.

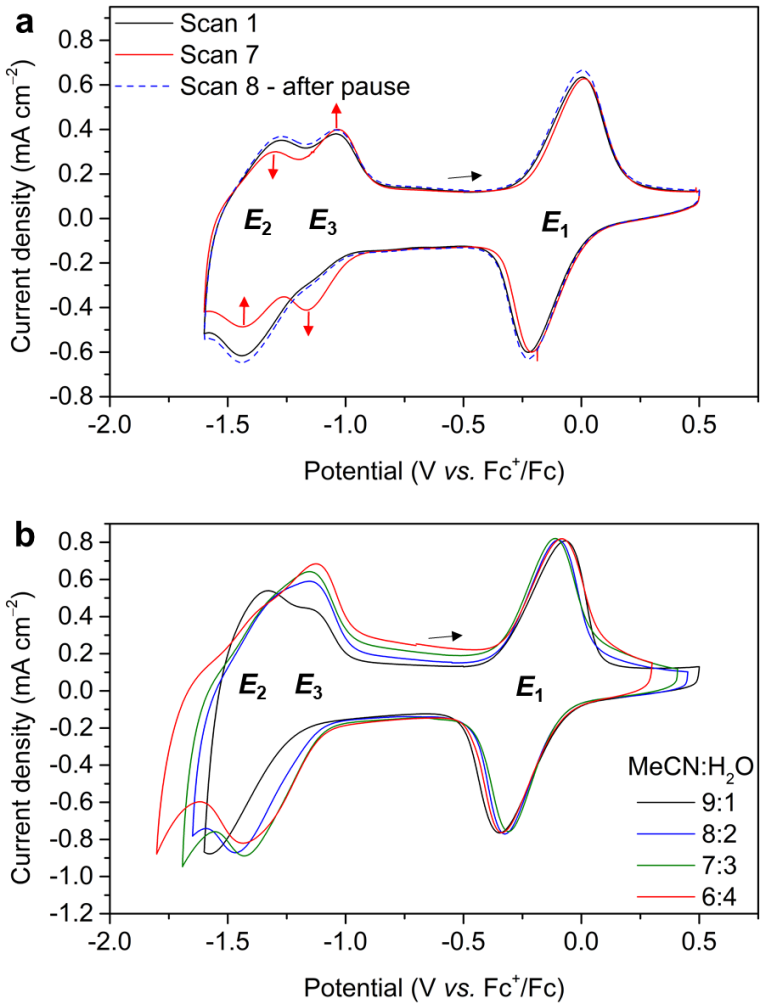

Figure 5. Cyclic voltammograms of mesoITO|**CotpyP**. (a) Consecutive CV scans of mesoITO|**CotpyP** in 9:1 MeCN:H_2O (0.1 M $TBABF_4$) with scans 1 and 7 being shown (red arrows indicate change in wave intensities); scan 8 was recorded after a pause at open circuit potential. (b) CV scans of mesoITO|**CotpyP** in MeCN:H_2O ratios of 9:1, 8:2, 7:3 and 6:4 (0.1 M $TBABF_4$), with scan 1 shown. Black arrows indicate scan start. Conditions: v = 50 mV s^{-1}; N_2 atmosphere; room temperature.

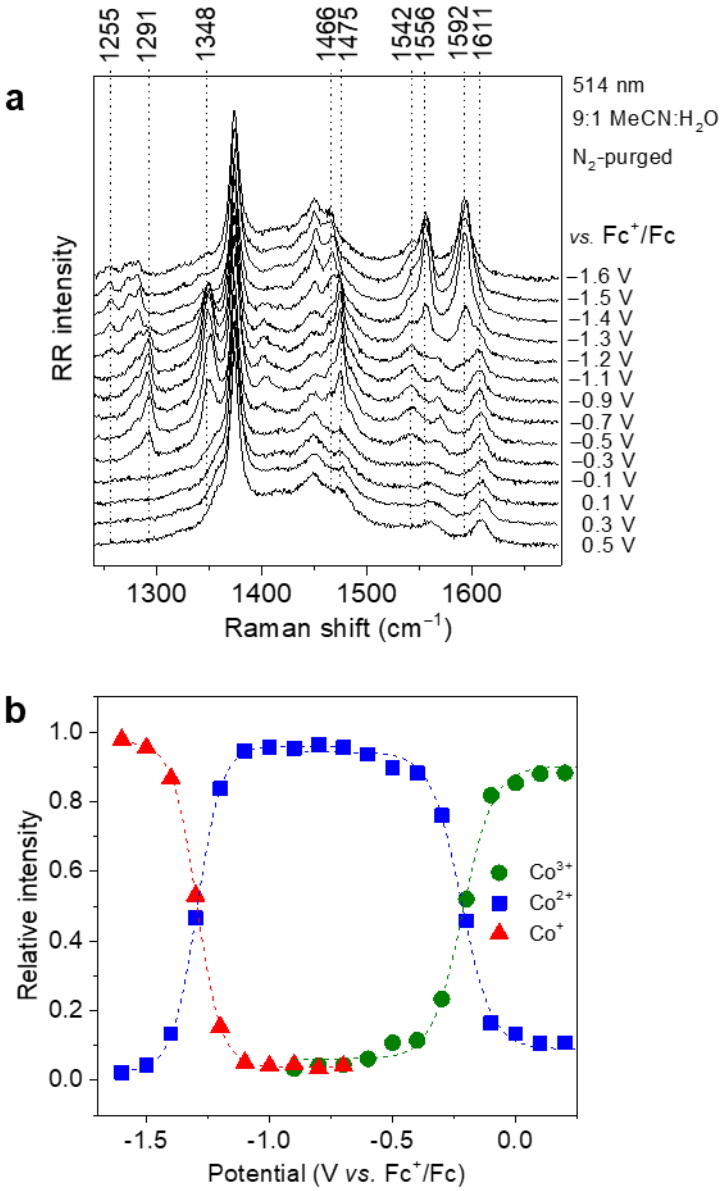

Figure 6. Confocal RR spectroelectrochemistry of mesoITO|**CotpyP**. (a) RR spectra at different E_{app}. (b) Relative intensities of the Co^{3+}, Co^{2+} and Co^{+} redox species as a function of E_{app}, with inflection points at −0.18 and −1.32 V *vs.* Fc^{+}/Fc. The relative intensities were derived using component fit analysis of the RR spectra (Supplementary Figure 22). Conditions: 9:1 MeCN:H_2O (0.1 M $TBABF_4$, N_2) at room temperature, λ_{ex} = 514 nm. Note that due to the intrinsically lower RR activity of Co^{3+} and Co^{2+} species causing an inaccuracy in the calculation procedure of about 10%, the relative intensities of Co^{2+} and Co^{3+} at positive potentials do not reach full redox conversion conditions, *i.e.* 0 and 1, respectively.

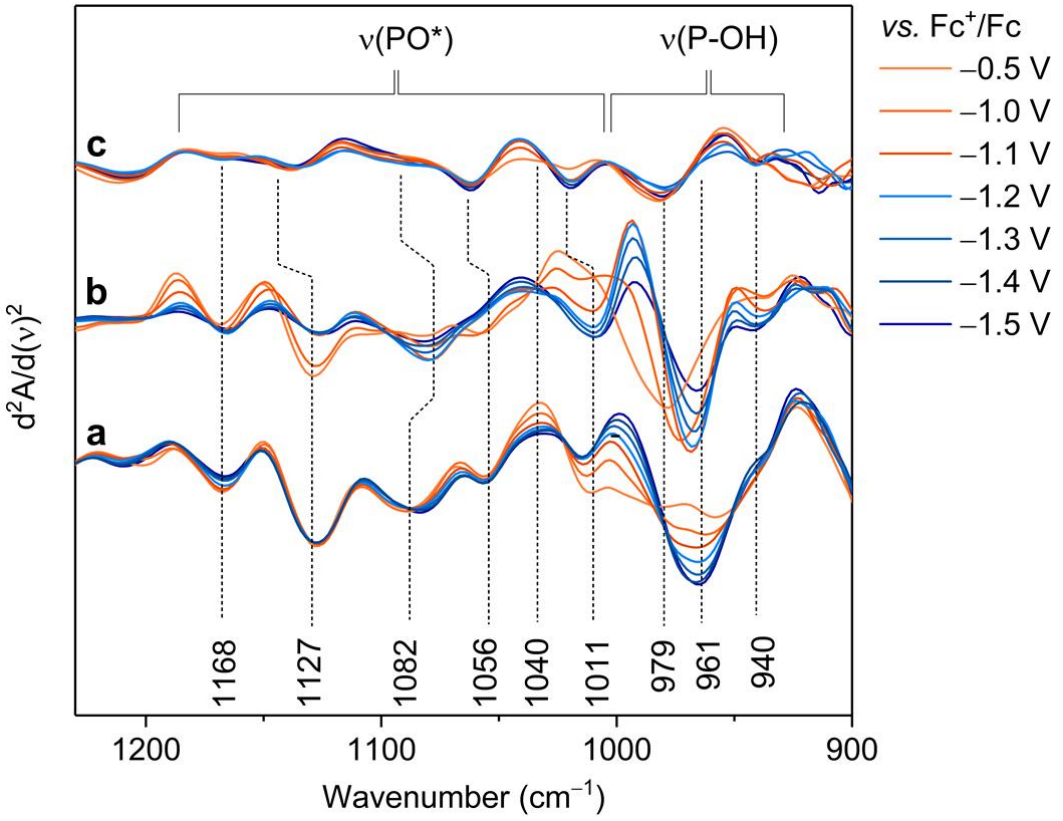

Figure 7. ATR-IR spectroelectrochemistry of immobilised **CotpyP**. Second derivatives of ATR-IR absorbance spectra in the phosphonate spectral region taken of mesoITO|**CotpyP** at different E_{app} (Supplementary Figure 26) in (a) N_2-purged MeCN, (b) N_2-purged 9:1 MeCN:H_2O and (c) CO_2-purged 9:1 MeCN:H_2O (0.1 M $TBABF_4$ in all cases) at room temperature. All spectra have been referenced to background spectra recorded from catalyst-free mesoITO for each of the above conditions. * indicates contributions from all possible P–O single bonds.

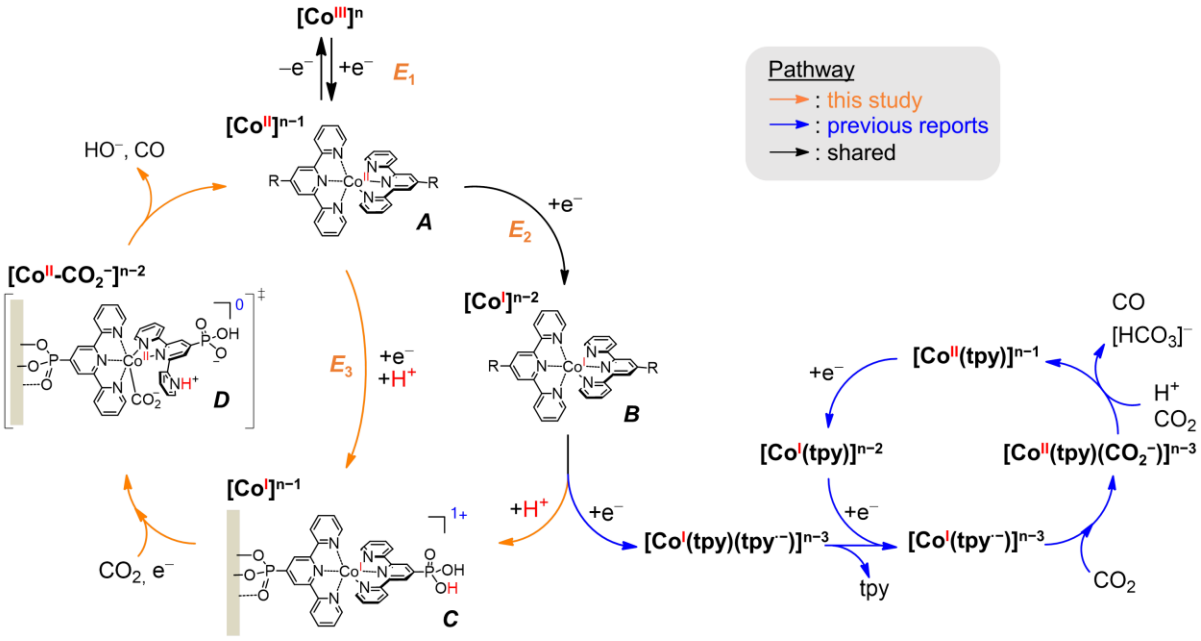

Figure 8. Proposed CO_2 reduction catalytic mechanism for immobilised **CotpyP**. Proposed catalytic mechanism and postulated intermediates for CO_2-to-CO reduction for immobilised **CotpyP** compared to the previously reported pathway for homogenous $[Co(tpy)_2]^{2+}$ (adapted from ref. 23). $\boldsymbol{E_1}$-$\boldsymbol{E_3}$ refer to potentials recorded in 9:1 MeCN:H_2O solutions of the indicated redox couples in this study. R in **A** and **B** is respective to individual reports (this work and ref. 24). It is noted that alternative CO_2-reducing mechanisms with a bis(terpyridine) ligation cannot be entirely ruled out based on our data.

METHODS

Materials

Chemicals purchased for analytical measurements were of the highest available purity. Boron-doped Si wafers (resistivity of 1-10 ohm·cm; <100>; 500 μm thickness; single-side polished) were purchased from University Wafer. Ti foil (0.25 mm thick, 99.5 %) was purchased from Alfa Aesar. The TiO_2 paste was purchased from Solaronix (15-20 nm, Ti-Nanoxide T/SP, 100% anatase). Fluorine-doped tin oxide (FTO)-coated glass sheets were purchased from Sigma Aldrich (SnO_2/F, 7 Ω sq^{-1} sheet resistance, 300 × 300 × 2 mm). ITO nanopowder (< 50 nm particle size; BET = 27 m^2 g^{-1}; 90% In_2O_3, 10% SnO_2) was obtained from Sigma Aldrich. $KHCO_3$ and $Co(BF_4)_2{\cdot}6H_2O$ (96%) were purchased from Alfa Aesar and 2,2':6',2"-terpyridine-4'-phosphonic acid was purchased from HetCat, Switzerland (98%). $TBABF_4$ was purchased from Sigma Aldrich (≥ 99.0%, electrochemical grade). MeOH and MeCN were both distilled over calcium hydride before use. All aqueous experimental solutions were prepared with ultrapure water (DI water; Milli-Q®, 18.2 MΩ cm). $^{13}CO_2$ (> 99 atom % ^{13}C) was purchased from Sigma Aldrich. Mono(terpyridine) [$CoCl_2$(tpy)] was prepared following a previously-reported procedure.[54]

Physical Characterisation

^1H and ^{31}P NMR spectra were recorded on a Bruker 500 MHz DCH cryoprobe spectrometer at room temperature. Chemical shifts are given in ppm and coupling constants in Hz. Chemical shifts for ^1H NMR spectra are referenced relative to residual protium in the deuterated methanol (Eurisotop). High resolution-mass spectra were recorded using a ThermoScientific Orbitrap Classic mass spectrometer. UV-vis spectra were collected using a Varian Cary 50 Bio UV-vis spectrometer. For solution spectra, a quartz cuvette (Hellma, 1 cm path length) was used. ATR-FTIR spectra were recorded on a Nicolet iS50 spectrometer. Elemental analysis was carried out by the Microanalysis Service of the Department of Chemistry, University of Cambridge, using a Perkin-Elmer 240 Elemental Analyser.

Inductively coupled plasma optical emission spectrometry (ICP-OES) measurements were conducted by the Microanalysis Service of the Department of Chemistry, University of Cambridge, on a Thermo Scientific iCAP 7400 ICP-OES DUO spectrometer. XPS was performed on a Thermo Fisher Scientific K-alpha$^+$ spectrometer using a micro-focused monochromatic Al X-ray source (72 W) over an area of approximately 400 microns, with argon sputtering performed using a Thermo Scientific MAGCIS source operating in the monatomic mode at 4 kV over a raster area of approximately 2 mm^2. Data analysis was performed in CasaXPS using a Shirley type background and Scofield cross sections, with an energy dependence of −0.6.

Synthesis and Characterisation of CotpyP Catalyst

2,2':6',2"-terpyridine-4'-phosphonic acid (**tpyP**; 30.0 mg, 9.6×10^{-5} mol) and $Co(BF_4)_2\cdot6H_2O$ (14.3 mg, 4.2×10^{-5} mol) were placed in a round bottom flask under N_2 atmosphere and solubilised with 6 mL of MeOH (a few drops of water can be added to improve the solubility). The solution was stirred for 24 h at room temperature during which the colour gradually turned from colourless to red-brown, attesting to the formation of the cobalt bis(terpyridine) complex. 4 mL of ethanol was then added, followed by ethyl acetate to precipitate the complex. The solid was filtered off on Millipore and washed with ethyl acetate. The solid was dried under vacuum to afford 21 mg of **CotpyP** complex as a fine brown powder (58%). ^{1}H NMR (MeOD, 500 MHz): δ_H (ppm) = 91.00 (bs, H^5), 52.39 (s, H^2), 38.82 (s, H^4), 32.86 (s, H^1), 9.74 (s, H^3) (assignment based on ref. 12); ^{31}P NMR (MeOD, 202 MHz): δ_P (ppm) = 34.25; FT-IR (ATR): σ (cm^{-1}): 1604, 1558, 1480, 1416, 1166, 1140. HRMS (+ESI, m/z): calcd. for $C_{30}H_{23}O_6N_6{}^{56}Co_1P_2$ $[M-H^+-2\cdot BF_4^-]^+$: 684.0481; found, 684.0472. Anal. calcd. for $C_{30}H_{24}B_2Co_1F_8N_6O_6P_2$: C, 41.95; H, 2.82; N, 9.78; P, 7.21; found: C, 41.76; H, 3.22; N, 9.57; P, 7.32. UV-vis. (MeOH): λ_{max} (nm) = 320, 448, 510, 555.

Fabrication of mesoITO Electrode

FTO-coated glass sheets were cut into 1 cm × 3 cm pieces and cleaned by immersing them in a solution of water, ammonia (35%, Fisher Scientific) and hydrogen peroxide (30% w/v, Breckland Scientific Supplies) in a 5:1:1 v/v ratio at 70 °C for 30 min. The glass slides were subsequently sonicated in water and dried at room temperature. An ITO suspension consisting of 20 wt % of ITO nanopowder (particle size < 50 nm) in 5 M acetic acid in ethanol was prepared and sonicated well. This was spin-coated onto the cleaned FTO glass slides over a 1 × 0.8 cm area defined using Scotch® tape (3M) as spacers, using a volume of 200 µL per slide and a spin speed of 1000 rpm over 1 min. The solution was left to dry completely in air before removing the tape and annealing in a Carbolite furnace under atmospheric conditions using the following temperature program: heating from 25 °C to 400 °C (5 °C min^{-1}), holding at 400 °C for 30 min before slowly cooling down to room temperature in the furnace chamber.

Fabrication of Si|mesoTiO$_2$ Electrode

The preparation of the Si|mesoTiO$_2$ electrode (TiO$_2$ layer thickness ≈ 6 µm) was conducted following a previously reported procedure.[15] In brief, the Si wafer is etched with HF acid, followed by immediate deposition and sintering of a mesoTiO$_2$ film.

Fabrication of Ti|mesoTiO$_2$ Electrode

The Ti foil (10 × 20 × 0.25 mm) was sonicated sequentially in isopropanol and ethanol for 30 min, and dried under a flow of N_2. Subsequent deposition of the mesoTiO$_2$ film was conducted in the same manner as that on Si to make Si|mesoTiO$_2$ electrodes (above).

Assembly of CotpyP mesoITO, Ti|mesoTiO$_2$ and Si|mesoTiO$_2$

Immobilisation of **CotpyP** on mesoITO, Ti|mesoTiO$_2$ or Si|mesoTiO$_2$ was carried out by soaking the electrodes in a methanolic solution of **CotpyP** (prepared by the dropwise addition of a MeOH solution of **tpyP** to a MeOH solution of $Co(BF_4)_2 \cdot 6H_2O$ to give a final concentration of 0.25 mM) for 16 h. The mesoITO|**CotpyP**, Ti|mesoTiO$_2$|**CotpyP** and Si|mesoTiO$_2$|**CotpyP** electrodes were rinsed with MeOH and dried prior to use. In the case of the control experiment using a Si|mesoTiO$_2$|$Co(BF_4)_2$ electrode, a solution of the $Co(BF_4)_2 \cdot 6H_2O$ salt (0.25 mM) was used to sensitise the Si|mesoTiO$_2$ electrode instead of **CotpyP**.

In the case of Ti|mesoTiO$_2$|**CotpyP** and Si|mesoTiO$_2$|**CotpyP**, the photocathodes were subsequently back-contacted and insulated by an epoxy adhesive prior to further use. Sand paper was used to abrade the back of the electrodes (unpolished Si side for Si electrodes) before application of a conductive silver paint (RS® Components 186-3593), after which an electrical wire was connected to the dry silver using the same conductive silver paint. Upon drying, an off-white opaque epoxy adhesive (Loctite® EA 9466) was applied on both sides of the electrodes, leaving only the photoactive surface ($S \approx 0.2$ cm^2) exposed. The cells were allowed to dry thoroughly for 40 h in air before use.

Quantification of Catalyst Loading

The quantification of the amount of immobilised **CotpyP** (mole per geometrical area) on the Si|mesoTiO$_2$|**CotpyP** electrodes was evaluated in triplicate by inductively coupled plasma optical emission spectrometry (ICP-OES) after digestion of Si|mesoTiO$_2$|**CotpyP** electrodes (≈ 1 cm^2 film area) in aqueous HNO_3 (70%) overnight and dilution to 2% v/v with MilliQ® water.

Electrochemistry

Electrochemical experiments were performed with an Ivium CompactStat potentiostat. A three-electrode configuration was employed in airtight compartments, with a Pt mesh as the counter electrode (CE) and a Ag/AgCl electrode in either saturated $KCl_{(aq.)}$ for aqueous experiments or in a solution with the same composition as the electrolyte for organic-water mixture experiments as the reference electrode (RE). In organic-water mixtures, the RE was regularly referenced against the ferrocene couple (Fc^+/Fc). Variations in the potential of the Fc^+/Fc couple in different solvent mixtures were taken into account.[55] The electrolyte was tetrabutylammonium tetrafluoroborate (0.1 M) in organic-water mixtures and $KHCO_3$ (0.1 M) in aqueous solutions. All electrochemical measurements were performed at room temperature.

CV scans were recorded with mesoITO-based working electrodes (WE) in the dark in one-compartment cells. The electrolyte solution was purged with either N_2 or CO_2 for 15 min to remove atmospheric O_2.

LSVs and CP(P)E were performed on Ti|mesoTiO$_2$- and Si|mesoTiO$_2$-based electrodes as the working electrodes, the former in the dark and the latter under illumination. A Newport Oriel Xenon 150 W solar light simulator (100 mW cm^{-2}, AM1.5G containing IR water and UV (λ < 400 nm) filters) was used as the light source in the case of Si|mesoTiO$_2$-based electrodes; an additional neutral density filter was used in the case of light intensity dependence LSV studies on Si|mesoTiO$_2$|**CotpyP** to vary the light intensity between 0-100% of 1 Sun.

Custom-made airtight two-compartment photoelectrochemical cells were employed for all (photo)electrochemical measurements, where a glass frit or Nafion membrane was used to separate the compartments for organic-water mixtures or aqueous solutions, respectively. LSVs were conducted at a scan rate of 5 mV s^{-1}, with chopped light alternating between dark and light every 5 s for Si|mesoTiO$_2$|**CotpyP** electrodes. E_{cat} was defined as the potential at which a photocurrent density of $|J|$ = 10 μA cm^{-2} was achieved by the respective

electrode. The applied potential during CPPE was −1.0 V *vs.* Fc^+/Fc or 0.0 V *vs.* RHE in organic-water or pure water solutions, respectively. Continuous illumination was maintained, apart from hourly dark chops lasting for 2 min each. The applied potential during CPE in the dark on Ti|mesoTiO$_2$-based electrodes was varied between −1.0, −1.2, −1.3 and −1.4 V *vs.* Fc^+/Fc.

Prior to all (photo)electrochemical experiments, the electrolyte solution in both compartments of the photoelectrochemical cell was purged with CO_2 containing 2% CH_4 as an internal standard for gas chromatography measurements; the only exception was in the case of N_2 atmosphere control experiments, where the solution was purged with N_2 containing 2% CH_4. The amount of gaseous CO and H_2 produced was analysed by headspace gas analysis using a Shimadzu Tracera GC-2010 Plus with a barrier discharge ionization detector (BID). The GC was equipped with a ShinCarbon micro ST column (0.53 mm diameter) kept at 40 °C using helium carrier gas. Aliquots (50 µL) of the headspace gas were removed from the sealed photoelectrochemical vessel using a gastight syringe (Hamilton, GASTIGHT®) for GC analysis at hourly time intervals. Formic acid was analysed by ion chromatography using a Metrohm 882 compact IC plus ion chromatography system, with a solution of carbonate (4 mM) containing acetone (50 mL L^{-1}) as the eluent after calibration with solutions of different known formate concentrations. The FE of the photocathodes was calculated by comparing the expected amount of total product as indicated by the total charge passed through the electrode and the actual amount produced. Analytical measurements were performed in triplicate and the standard deviation of each data point is given in the supporting tables and denoted by error bars in the graphs.

Isotopic Labelling

CPPE of the Si|mesoTiO$_2$|**CotpyP** electrode was performed under 6:4 MeCN:H_2O conditions with $^{13}CO_2$ as the headspace gas. After 4 h, the photoelectrochemical cell headspace was

transferred to an evacuated gas IR cell (SpecAc, 10 cm path length, equipped with KBr windows) and a high-resolution transmission spectrum was collected on a Thermo Scientific Nicolet iS50 FT-IR spectrometer.

Spectroelectrochemical Resonance Raman Spectroscopy

RR measurements of mesoITO|**CotpyP** were carried out using the 413 nm line of a Kr ion laser (Sabre), and the 458 nm and 514 nm lines of an Ar ion laser (Coherent Innova 300c). A Horiba LabRamII confocal Raman spectrometer equipped with a liquid nitrogen-cooled CCD detector (Symphony) was employed. The laser light was focused onto the sample using a 20× objective (Nikon, 20×, NA 0.05). Potentials during the Raman spectroscopic experiments were applied using a multichannel potentiostat (MetrOhm MicroAutoLab). Measurements were carried out in anhydrous MeCN or 9:1 MeCN:H_2O/9:1 MeCN:D_2O with 0.1 M $TBABF_4$ as electrolyte. As counter and reference electrodes, a hydrogen flame-cleaned Pt wire and a leak-free Ag/AgCl in 0.1 M H_2SO_4 (DriRef, WPI) were used, respectively. To acidify the 9:1 MeCN:D_2O mixture, DCl was added (final concentration: 95 µM). The samples were moved during measurements using an xy-stage (OWISoft) to avoid laser-induced sample degradation.

Analysis of the spectra was performed using a home-made software (Qpipsi) and component fitting analyses were performed following published procedures.[39,56] To derive the component spectra, RR spectra of mesoITO|**CotpyP** using 514 nm excitation recorded at very positive (0.5 V *vs.* Fc^+/Fc), intermediate (−0.5 V *vs.* Fc^+/Fc) and very negative potentials (−1.5 V *vs.* Fc^+/Fc) were considered first. These spectra were each expected to be spectrally dominated by the **CotpyP** species in only one oxidation state ([$\mathbf{Co^{III}}$], [$\mathbf{Co^{II}}$] and [$\mathbf{Co^{I}}$], respectively). The spectra were iteratively fitted using Lorentzian bands by iteratively varying their absolute intensity, half-width and frequency until a full reproduction of the spectra was achieved. The resulting bands were grouped to afford a component spectrum,

i.e. three spectra were derived in total. RR spectra measured at intermediate potentials were finally fitted using the so-derived component spectra allowing only a variation by a fitting parameter factor *GF*, *i.e.* varying spectral contribution of a respective component spectrum to overall RR spectrum.

Group intensities were obtained by multiplying *GF* with a prominent, highly intense band found in the respective component spectrum to obtain the intensity of the respective *i* component spectrum I_i. Relative intensities $I_{i,rel}$ for a component spectrum *i* were calculated using:

$$I_{i,rel} = \frac{I_i}{\left(\sum_f I_f\right)}$$

Spectroelectrochemical Infrared Spectroscopy

Spectroelectrochemical ATR-IR measurements were carried out on mesoITO|**CotpyP** prepared on a Si ATR prism. An ITO suspension consisting of 10 wt % of ITO nanopowder in 5 M acetic acid in ethanol was prepared and sonicated well. This was spin-coated onto the flat surface of the Si ATR-prism over the complete area of 3 cm², using a volume of 50 µL and a spin speed of 1000 rpm over 1 minute. The solution was left to dry completely in air before annealing at 400 °C for 30 min (5 °C min^{-1}) under atmospheric conditions. **CotpyP** was adsorbed from 1 mL of the catalyst stock solution in MeOH (0.25 mM) for 45 min at room temperature. After the adsorption process was completed, the catalyst solution was removed from the ATR cell and the electrode rinsed several times with MeOH.

Spectroelectrochemical ATR-IR measurements were performed in a single-reflection PIKE ATR-IR setup and a customised ATR -IR spectroelectrochemical cell using an angle of incidence of 60°. The electrochemical studies were carried out in a three-electrode system with the mesoITO|**CotpyP** film as WE, a Ag/AgCl electrode (in a solution with the same composition as the electrolyte) as RE, and a Pt wire as CE. Potentials were applied using an Ivium CompactStat potentiostat. The ATR-IR spectra were recorded in a spectral range from 4000 to 900 cm^{-1} (note that the range below 900 cm^{-1} is inaccessible due to strong

absorption by the Si ATR prism) with a spectral resolution of 4 cm^{-1} on a Bruker Vertex 70 spectrometer equipped with a photovoltaic MCT detector. A total of 200 scans were co-added for one spectrum, requiring an accumulation time of 1.5 min. All measurements were carried out at room temperature under either N_2 or CO_2 overpressure.

ATR-IR spectra were evaluated using the OPUS 5.5 software. Absorbance spectra (A) were generated according to the Lambert−Beer equation:

$$A = -log \frac{I_{sample}}{I_{reference}}$$

I_{sample} denotes the sample spectrum and $I_{reference}$ denotes the respective reference spectrum for absorbance spectra. Baseline corrections of the absorbance spectra and second derivative spectra were generated by means of the OPUS 5.5 software data analysis tools.

DATA AVAILABILITY

The data that support the plots within this paper and other findings of this study are available from the corresponding author upon reasonable request.

References

1 Detz, R. J., Reek, J. N. H. & van der Zwaan, B. C. C. The future of solar fuels: when could they become competitive? *Energy Environ. Sci.* **11**, 1653-1669 (2018).

2 Appel, A. M. *et al.* Frontiers, opportunities, and challenges in biochemical and chemical catalysis of CO_2 fixation. *Chem. Rev.* **113**, 6621-6658 (2013).

3 Takeda, H., Cometto, C., Ishitani, O. & Robert, M. Electrons, Photons, Protons and Earth-Abundant Metal Complexes for Molecular Catalysis of CO_2 Reduction. *ACS Catal.* **7**, 70-88 (2016).

4 Zhang, L., Zhao, Z.-J., Wang, T. & Gong, J. Nano-designed semiconductors for electro- and photoelectro-catalytic conversion of carbon dioxide. *Chem. Soc. Rev.* **47**, 5423-5443 (2018).

5 Dalle, K. E. *et al.* Electro- and Solar-Driven Fuel Synthesis with First Row Transition Metal Complexes. *Chem. Rev.*, 10.1021/acs.chemrev.1028b00392 (2019).

6 Arai, T. *et al.* Photoelectrochemical reduction of CO_2 in water under visible-light irradiation by a p-type InP photocathode modified with an electropolymerized ruthenium complex. *Chem. Commun.* **46**, 6944-6946 (2010).

7 Sato, S. *et al.* Selective CO_2 conversion to formate conjugated with H_2O oxidation utilizing semiconductor/complex hybrid photocatalysts. *J. Am. Chem. Soc.* **133**, 15240-15243 (2011).

8 Sahara, G. *et al.* Photoelectrochemical Reduction of CO_2 Coupled to Water Oxidation Using a Photocathode With a Ru(II)-Re(I) Complex Photocatalyst and a CoOx/TaON Photoanode. *J. Am. Chem. Soc.* **138**, 14152-14158 (2016).

9 Kumagai, H. *et al.* Hybrid photocathode consisting of a $CuGaO_2$ p-type semiconductor and a Ru(II)-Re(I) supramolecular photocatalyst: non-biased visible-light-driven CO_2 reduction with water oxidation. *Chem. Sci.* **8**, 4242-4249 (2017).

10 Sekizawa, K., Sato, S., Arai, T. & Morikawa, T. Solar-Driven Photocatalytic CO_2 Reduction in Water Utilizing a Ruthenium Complex Catalyst on p-Type Fe_2O_3 with a Multiheterojunction. *ACS Catal.* **8**, 1405-1416 (2018).

11 Feldman, D. B. *et al.* Photovoltaic System Pricing Trends: Historical, Recent, and Near-Term Projections. (report NREL/PR-6A20-64898, NREL Laboratory, 2015). http://www.nrel.gov/docs/fy15osti/64898.pdf.

12 Constable, E. C., Harris, K., Housecroft, C. E., Neuburger, M. & Zampese, J. A. Environmental control of solution speciation in cobalt(II) 2,2':6',2''-terpyridine complexes: anion and solvent dependence. *Dalton Trans.* **40**, 11441-11450 (2011).

13 Potts, K. T., Usifer, D. A., Guadalupe, A. & Abruña, H. D. 4-Vinyl-, 6-vinyl-, and 4'-vinyl-2,2':6',2''-terpyridinyl ligands: their synthesis and the electrochemistry of their transition-metal coordination complexes. *J. Am. Chem. Soc.* **109**, 3961-3967 (1987).

14 Enachescu, C. *et al.* Optical investigation of spin-crossover in cobalt(II) bis-terpy complexes. *Inorg. Chim. Acta* **360**, 3945-3950 (2007).

15 Leung, J. J. *et al.* Photoelectrocatalytic H_2 evolution in water with molecular catalysts immobilised on p-Si via a stabilising mesoporous TiO_2 interlayer. *Chem. Sci.* **8**, 5172-5180 (2017).

16 Guerrero, G., Mutin, P. H. & Vioux, A. Organically modified aluminas by grafting and sol–gel processes involving phosphonate derivatives. *J. Mater. Chem.* **11**, 3161-3165 (2001).

17 Bae, E. *et al.* Effects of Surface Anchoring Groups (Carboxylate vs Phosphonate) in Ruthenium-Complex-Sensitized TiO_2 on Visible Light Reactivity in Aqueous Suspensions. *J. Phys. Chem. B* **108**, 14093-14101 (2004).

18 Fuchs, P., Hess, U., Holst, H. H. & Lund, H. Electrochemical Carboxylation of Some Heteroaromatic Compounds. *Acta Chem. Scand. B* **35b**, 185-192 (1981).

19 Li, Y.-F., Aschauer, U., Chen, J. & Selloni, A. Adsorption and Reactions of O_2 on Anatase TiO_2. *Acc. Chem. Res.* **47**, 3361-3368 (2014).

20 Seger, B. *et al.* Using TiO_2 as a Conductive Protective Layer for Photocathodic H_2 Evolution. *J. Am. Chem. Soc.* **135**, 1057-1064 (2013).
21 Elgrishi, N., Chambers, M. B., Artero, V. & Fontecave, M. Terpyridine complexes of first row transition metals and electrochemical reduction of CO_2 to CO. *Phys. Chem. Chem. Phys.* **16**, 13635-13644 (2014).
22 Cobo, S. *et al.* A Janus cobalt-based catalytic material for electro-splitting of water. *Nat. Mater.* **11**, 802-807 (2012).
23 Chuang, T. J., Brundle, C. R. & Rice, D. W. Interpretation of the x-ray photoemission spectra of cobalt oxides and cobalt oxide surfaces. *Surf. Sci.* **59**, 413-429 (1976).
24 Matsubara, Y. Standard Electrode Potentials for the Reduction of CO_2 to CO in Acetonitrile–Water Mixtures Determined Using a Generalized Method for Proton-Coupled Electron-Transfer Reactions. *ACS Energy Lett.* **2**, 1886-1891 (2017).
25 Perry, R. H. *Perry's Chemical Engineers' Handbook*. 8th ed. edn, (New York ; London : McGraw-Hill, c2008., 2008).
26 Heinzel, A. B., Teschner, D. M. & Schumacher, R. Influence of Water on the Capacitance/Potential Distribution at the TiO_2/CH_3CN Junction. *Ber. Bunsenges. Phys. Chem.* **85**, 1117-1119 (1981).
27 Sumita, M., Sodeyama, K., Han, L. & Tateyama, Y. Water Contamination Effect on Liquid Acetonitrile/TiO_2 Anatase (101) Interface for Durable Dye-Sensitized Solar Cell. *J. Phys. Chem. C* **115**, 19849-19855 (2011).
28 Enright, B., Redmond, G. & Fitzmaurice, D. Spectroscopic determination of flatband potentials for polycrystalline TiO_2 electrodes in mixed solvent systems. *J. Phys. Chem.* **98**, 6195-6200 (1994).
29 Won, D. I. *et al.* Highly Robust Hybrid Photocatalyst for Carbon Dioxide Reduction: Tuning and Optimization of Catalytic Activities of Dye/TiO_2/Re(I) Organic-Inorganic Ternary Systems. *J. Am. Chem. Soc.* **137**, 13679-13690 (2015).
30 Sahara, G. *et al.* Photoelectrochemical CO_2 reduction using a Ru(II)-Re(I) multinuclear metal complex on a p-type semiconducting NiO electrode. *Chem. Commun.* **51**, 10722-10725 (2015).
31 Apaydin, D. H. *et al.* Photoelectrochemical Reduction of CO_2 Using Third-Generation Conjugated Polymers. *ChemistrySelect* **1**, 1156-1162 (2016).
32 Schreier, M. *et al.* Covalent Immobilization of a Molecular Catalyst on Cu_2O Photocathodes for CO_2 Reduction. *J. Am. Chem. Soc.* **138**, 1938-1946 (2016).
33 Kumar, B., Smieja, J. M. & Kubiak, C. P. Photoreduction of CO_2 on p-type Silicon Using Re(bipy-Bu^t)$(CO)_3Cl$: Photovoltages Exceeding 600 mV for the Selective Reduction of CO_2 to CO. *J. Phys. Chem. C* **114**, 14220-14223 (2010).
34 Alenezi, K., Ibrahim, S. K., Li, P. & Pickett, C. J. Solar fuels: photoelectrosynthesis of CO from CO_2 at p-type Si using Fe porphyrin electrocatalysts. *Chem. Eur. J.* **19**, 13522-13527 (2013).
35 Torralba-Peñalver, E., Luo, Y., Compain, J.-D., Chardon-Noblat, S. & Fabre, B. Selective Catalytic Electroreduction of CO_2 at Silicon Nanowires (SiNWs) Photocathodes Using Non-Noble Metal-Based Manganese Carbonyl Bipyridyl Molecular Catalysts in Solution and Grafted onto SiNWs. *ACS Catal.* **5**, 6138-6147 (2015).
36 Elgrishi, N., Chambers, M. B., Wang, X. & Fontecave, M. Molecular polypyridine-based metal complexes as catalysts for the reduction of CO_2. *Chem. Soc. Rev.* **46**, 761-796 (2017).
37 Šloufová, I., Vlčková, B., Procházka, M., Svoboda, J. & Vohlídal, J. Comparison of SERRS and RRS excitation profiles of $[Fe(tpy)_2]^{2+}$ (tpy = 2,2':6',2''-terpyridine) supported by DFT calculations: effect of the electrostatic bonding to chloride-modified Ag nanoparticles on its vibrational and electronic structure. *J. Raman Spectrosc.* **45**, 338-348 (2014).
38 Keidel, A. *et al.* Electrochemical and Resonance Raman Spectroscopic Studies of Water-Oxidizing Ruthenium Terpyridyl–Bipyridyl Complexes. *ChemSusChem* **10**, 551-561 (2017).

39 Ly, H. K. *et al.* 2nd coordination sphere controlled electron transfer of iron hangman complexes on electrodes probed by surface enhanced vibrational spectroscopy. *Chem. Sci.* **6**, 6999-7007 (2015).
40 Hugot-Le Goff, A., Joiret, S. & Falaras, P. Raman Resonance Effect in a Monolayer of Polypyridyl Ruthenium(II) Complex Adsorbed on Nanocrystalline TiO_2 via Phosphonated Terpyridyl Ligands. *J. Phys. Chem. B* **103**, 9569-9575 (1999).
41 Sun, Y. *et al.* Molecular Cobalt Pentapyridine Catalysts for Generating Hydrogen from Water. *J. Am. Chem. Soc.* **133**, 9212-9215 (2011).
42 Yaguchi, M., Uchida, T., Motobayashi, K. & Osawa, M. Speciation of Adsorbed Phosphate at Gold Electrodes: A Combined Surface-Enhanced Infrared Absorption Spectroscopy and DFT Study. *J. Phys. Chem. Lett.* **7**, 3097-3102 (2016).
43 Arai, Y. & Sparks, D. L. ATR–FTIR Spectroscopic Investigation on Phosphate Adsorption Mechanisms at the Ferrihydrite–Water Interface. *J. Colloid Interface Sci.* **241**, 317-326 (2001).
44 Yoshida, T., Iida, T., Shirasagi, T., Lin, R.-J. & Kaneko, M. Electrocatalytic reduction of carbon dioxide in aqueous medium by bis(2,2′: 6′,2″-terpyridine)cobalt(II) complex incorporated into a coated polymer membrane. *J. Electroanal. Chem.* **344**, 355-362 (1993).
45 Rooth, M. & Shaw, A. M. Interfacial pH and surface p*K*a of a thioctic acid self-assembled monolayer. *Phys. Chem. Chem. Phys.* **8**, 4741-4743 (2006).
46 White, H. S., Peterson, J. D., Cui, Q. & Stevenson, K. J. Voltammetric Measurement of Interfacial Acid/Base Reactions. *J. Phys. Chem. B* **102**, 2930-2934 (1998).
47 Bjorneholm, O. *et al.* Water at Interfaces. *Chem. Rev.* **116**, 7698-7726 (2016).
48 He, T. *et al.* Electron trapping induced electrostatic adsorption of cations: a general factor leading to photoactivity decay of nanostructured TiO_2. *J. Mater. Chem. A* **5**, 6455-6464 (2017).
49 Aroua, S. *et al.* New Cobalt-Bisterpyridyl Catalysts for Hydrogen Evolution Reaction. *ChemCatChem* **9**, 2099-2105 (2017).
50 Guadalupe, A. R. *et al.* Novel chemical pathways and charge-transport dynamics of electrodes modified with electropolymerized layers of $[Co(v\text{-}terpy)_2]^{2+}$. *J. Am. Chem. Soc.* **110**, 3462-3466 (1988).
51 Veldkamp, B. S. *et al.* Photoinitiated multi-step charge separation and ultrafast charge transfer induced dissociation in a pyridyl-linked photosensitizer-cobaloxime assembly. *Energy Environ. Sci.* **6**, 1917-1928 (2013).
52 Nazeeruddin, M. K., Zakeeruddin, S. M., Humphry-Baker, R., Kaden, T. A. & Grätzel, M. Determination of p*K*a Values of 4-Phosphonato-2,2‘:6‘,2‘ ‘-Terpyridine and Its Ruthenium(II)-Based Photosensitizer by NMR, Potentiometric, and Spectrophotometric Methods. *Inorg. Chem.* **39**, 4542-4547 (2000).
53 Reuillard, B. *et al.* Tuning Product Selectivity for Aqueous CO_2 Reduction with a Mn(bipyridine)-pyrene Catalyst Immobilized on a Carbon Nanotube Electrode. *J. Am. Chem. Soc.* **139**, 14425-14435 (2017).
54 Hogg, R. & Wilkins, R. G. 57. Exchange studies of certain chelate compounds of the transitional metals. Part VIII. 2,2',2''-terpyridine complexes. *J. Chem. Soc.*, 341-350 (1962).
55 Lanning, J. A. & Chambers, J. Q. Voltammetric study of the hydrogen ion/hydrogen couple in acetonitrile/water mixtures. *Anal. Chem.* **45**, 1010-1016 (1973).
56 Ly, H. K. *et al.* Perturbation of the redox site structure of cytochrome c variants upon tyrosine nitration. *J Phys Chem B* **116**, 5694-5702 (2012).

Acknowledgements

We gratefully acknowledge support from the Woolf Fisher Trust in New Zealand (J.J.L.), the Christian Doppler Research Association (Austrian Federal Ministry for Digital and Economic Affairs and the National Foundation for Research, Technology and Development) and the OMV Group (J.W., M.F.K. and E.R.), an ERC Consolidator Grant 'MatEnSAP' (682833; N.H. and E.R.), the European Union's Horizon2020 research and innovation programme (Marie Sklodowska-Curie fellowship for K.H.L., GAN 701192) and the National Research Foundation *via* the Creative Research Initiative Center (Republic of Korea, Grant No. NRF-2015R1A3A2066191; D.H.N.). We thank Dr David Morgan (Cardiff Catalysis Institute, Cardiff University) for help with XPS measurements.

Competing Interests

The authors declare no competing interest.

Author Contributions

J.J.L., J.W. and E.R. conceived the research. J.W. synthesised and characterised **CotpyP**. J.J.L., J.W. and D.H.N. prepared the electrodes. J.J.L. and J.W. carried out physical characterisation of the electrodes, J.J.L. the (photo)electrochemical experiments, K.H.L. the spectroelectrochemical RR measurements, and N.H. and J.J.L. the spectroelectrochemical ATR-IR measurements. J.J.L., J.W., K.H.L., N.H. and E.R. analysed the data. M.F.K. carried out initial preliminary investigations on **CotpyP**. J.J.L., J.W., K.H.L., N.H., M.F.K. and E.R. contributed to the creation of the manuscript. E.R. supervised the work.